

Quantum control of spin qubits using nanomagnets

Mohamad Niknam^{1,2,6}, Md. Fahim F. Chowdhury^{3,6}, Md Mahadi Rajib³, Walid Al Misba³, Robert N. Schwartz⁴, Kang L. Wang⁴, Jayasimha Atulasimha^{3,5} & Louis-S. Bouchard^{1,2}

Single-qubit gates are essential components of a universal quantum computer. Without selective addressing of individual qubits, scalable implementation of quantum algorithms is extremely challenging. When the qubits are discrete points or regions on a lattice, selectively addressing magnetic spin qubits at the nanoscale remains a challenge due to the difficulty of localizing and confining a classical divergence-free field to a small volume of space. Herein we propose a technique for addressing spin qubits using voltage-control of nanoscale magnetism, exemplified by the use of voltage control of magnetic anisotropy. We show that by tuning the frequency of the nanomagnet's electric field drive to the Larmor frequency of the spins confined to a nanoscale volume, and by modulating the phase of the drive, single-qubit quantum gates with fidelities approaching those for fault-tolerant quantum computing can be implemented. Such single-qubit gate operations require only tens of femto-Joules per gate operation and have lossless, purely magnetic field control. Their physical realization is also straightforward using foundry manufacturing techniques.

¹Department of Chemistry and Biochemistry, University of California Los Angeles, 607 Charles E. Young Drive East, Los Angeles, CA 90095-1059, USA.

²Center for Quantum Science and Engineering, UCLA, Los Angeles, CA, USA. ³Department of Mechanical and Nuclear Engineering, College of Engineering, Virginia Commonwealth University, Richmond, VA 23284-3068, USA. ⁴Device Research Laboratory, Department of Electrical and Computer Engineering, UCLA, 420 Westwood Plaza, Engineering IV, Los Angeles, CA 90095, USA. ⁵Department of Electrical and Computer Engineering, Virginia Commonwealth University, Richmond, VA, USA. ⁶These authors contributed equally: Mohamad Niknam and Md. Fahim F. Chowdhury.

[✉]email: jatulasimha@vcu.edu; lsbouchard@ucla.edu

Current physical implementations of quantum processors utilize qubits based on trapped ions¹, neutral atoms², nuclear spins^{3–5}, topological qubits⁶, superconducting circuits⁷, quantum dots^{8,9}, semiconductor spin qubits¹⁰, NV centers in diamond¹¹ as well as solid-state qubits made from other color centers¹². Spin qubits were among the first experimental realizations towards proposed quantum processors due to their long coherence times and available control methods in magnetic resonance experiments^{4,5}. In order to build quantum devices with spin qubits, a scalable design that provides individual control and detection is needed^{9,13–15}.

Universal quantum computing can be achieved with a minimum set of quantum gates that allow for the implementation of arbitrary quantum algorithms¹⁶. A robust implementation of quantum gates combined with error correction codes is the current prescription for fault-tolerant quantum computing¹⁷. The creation of high-fidelity single and two-qubit gates remains a challenge in every implementation, especially those involving spin qubits that are spatially localized at the atomic to nanoscales. At those length scales, the selective control of spin qubits is demanding because of the difficulty in creating strong, localized control fields that affect only the qubits in the volume of interest, while minimizing cross-talk with neighboring regions.

In this work, we show that for an isolated electron system, individual control of spin qubits can be realized using nanomagnets. Nanoscale magnets present two key advantages in controlling spin qubits: (1) Unlike collective application of microwaves in magnetic resonance experiments, they allow for the application of highly localized magnetic fields that minimize the effect on neighboring qubits. (2) They offer an extremely energy efficient pathway for the control of qubits. This leverages spintronic methods for energy-efficient manipulation of magnetization through the use of spin-orbit-torque (SOT)^{18–20}, voltage control of magnetic anisotropy (VCMA)^{21–26}, strain mediated voltage control or “straintronic” based methods^{27–32} and other paradigms for voltage control of magnetism³³. Energy efficiency is achieved through voltage control, rather than current control, thereby avoiding current dissipation losses³⁴ (I^2R) associated with the generation of magnetic fields. For example, the energy dissipation per bit for VCMA³⁵ and voltage induced strain from a piezoelectric layer is less than 1 fJ and 100 aJ, respectively, making them 100 and 1,000 times more efficient than state-of-the-art spin-transfer torque (STT) methods³⁶, which consume ~ 100 fJ per bit³⁴. Thus, the use of VCMA in controlling the magnetization of nanomagnets^{37–41} results in an energy efficient method for controlling qubits. Another interesting candidate is strain-mediated voltage control. Prior work has shown that one can use surface acoustic waves to drive a magnetic film at resonance, which emits magnons in a wide frequency band, some of which produce microwaves that drive transitions in NV centers⁴². However, this does not result in coherent rotations of the qubits. More recently, coherent rotation of single spin qubits in a NV center⁴³ by spin-waves propagating adjacent to it has been demonstrated. Nanoscale manipulation of silicon qubits^{9,14,15} including of flying qubits¹³ have also been demonstrated.

Herein we demonstrate the feasibility of scalable, small footprint, high-fidelity, energy-efficient quantum gates based on VCMA. Here, we use electron spins with g -factor of 2.0 as a model system to simulate qubit dynamics in the presence of a static external field whose magnitude is comparable to the stray field of the nanomagnets. This intermediate-field regime is considered more challenging due to the more pronounced effects of spatial inhomogeneities (i.e. spatially varying Larmor frequency and axis of quantization) and the lack of rotating-wave approximation. We also consider control of qubit ensembles located in a

finite-size nanoscale volume, where field inhomogeneities degrade gate fidelity when averaged over the volume.

The choice of implementing nanoscale control of spin ensembles in this work is motivated by recent proposals^{44–52} for quantum entanglers, bona fide qubits, quantum sensing and quantum memory. In all cases, high fidelity gate operations are needed. However, this comes at a cost, as gates implemented by an ensemble of spins distributed over a volume would suffer lower gate fidelity due to field inhomogeneities. This is studied here to ensure that we derive the benefits of spin ensembles while still achieving high gate fidelities. We shall use the term “qubit volume” to refer to the mesoscopic region enclosing the spin ensemble of interest. In the rest of the paper, we perform simulations of magnetization dynamics in voltage controlled nanomagnets and spin dynamics in spins proximal to such nanomagnets. We show that the spins can be individually addressed and driven at their Larmor frequency by the magnetization dynamics of nanomagnets, to implement single-qubit gates with fidelities approaching those for fault-tolerant quantum computing.

Results and discussion

Voltage control of nanomagnets to apply control pulses to the qubit. The magnetization dynamics of the nanomagnets — as simulated by solving the Landau-Lifshitz-Gilbert (LLG) equation (see Methods section) — leads to a time varying induced magnetic field in the qubit volume (also assumed to be nanoscale). A schematic diagram of the simulation setup of the qubit volume ($5 \text{ nm} \times 5 \text{ nm} \times 1 \text{ nm}$) with a nanomagnet in each side is shown in Fig. 1a–c. The qubit volume consists of a planar array of 25 spins defined as s_{ij} (i , row number; j , column number) in each cell so that each spin is separated from its neighbor by 1 nm.

The nanomagnets that drive the Rabi oscillations in these spins by inducing a resonant AC magnetic field due to their magnetization dynamics are elliptical in shape and have length, $a = 60 \text{ nm}$, width, $b = 20 \text{ nm}$, and thickness, $t = 1 \text{ nm}$. Since the qubit volume is near-field as it is very close to the nanomagnets (distance is $\sim 10 \text{ nm}$, which is a fraction of the wavelength $\sim 15 \text{ cm}$), we calculate AC magnetic field at the qubit volume from the magnetostatic field induced by the nanomagnet, which changes as a function of time due to the magnetization dynamics.

The nanomagnets and the qubit volume are assumed to be placed in a uniform external magnetic field pointing along the direction of the z -axis. Due to perpendicular magnetic anisotropy (PMA) as well as the global bias magnetic field (along $+z$) the magnetization of the nanomagnets are out-of-plane (and points along $+z$). To alter the magnetizations of the two identical nanomagnets, PMA is varied through the application of VCMA.

Note that in our case, the VCMA makes the in-plane direction easy, the shape anisotropy due to elliptical nanomagnet shape drives the magnetization to the easy (either $\pm x$) axis of the nanomagnet with equal probability⁵³. To preferentially orient the magnetization along $+x$, an exchange bias from an underlying antiferromagnet (AFM) can be applied, resulting in a highly localized exchange bias field, $B_{\text{bias},x}^{\text{ext}}$ along $(+x)$ in each nanomagnet. This exchange bias field can be realized at a ferromagnet/antiferromagnet (e.g., CoFeB/IrMn) interface as shown in Fig. 1b. The rotation of the magnetization to the $+x$ -direction due to VCMA induces a magnetic field along $+x$ in the qubit volume, which is located between the two nanomagnets with a distance of 10 nm from each of them indicated as d in Fig. 1a. The magnetization is restored to the z -direction when the PMA is increased.

By applying a sinusoidal voltage to the nanomagnets to induce VCMA, a periodic (sinusoidal with higher harmonics due to nonlinear response) magnetic field is induced along x -axis which is applied to the spins in the qubit volume and causes Larmor precession of these spins when frequency of this induced field

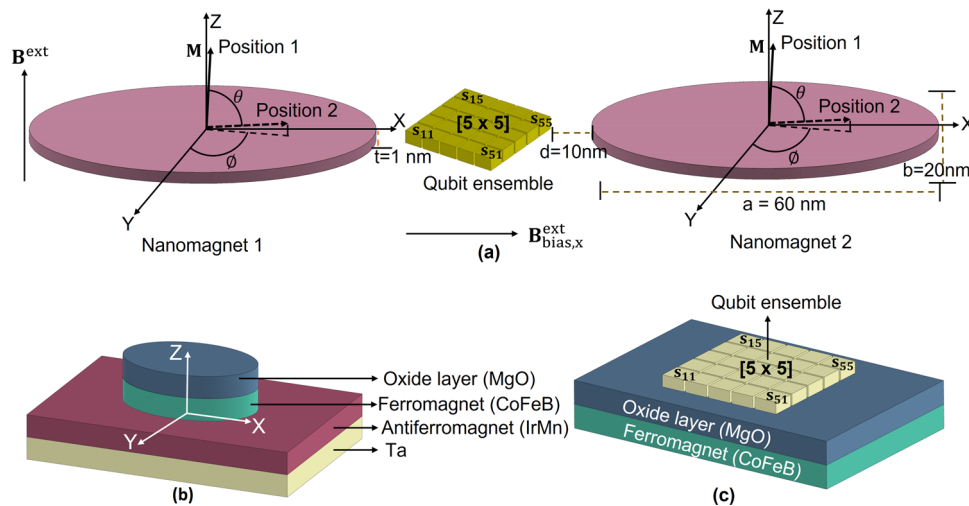


Fig. 1 Geometry (setup) of nanomagnets and qubits. **a** Schematic diagram of simulation setup in MuMax3. **b** Schematic of nanomagnet layers. Ferromagnet/antiferromagnet interface creates exchange bias field ($\mathbf{B}_{\text{bias},x}^{\text{ext}}$) along the $+x$ direction in the nanomagnet. The field deterministically oscillates from $+z$ to $+x$ when voltage-controlled magnetic anisotropy (VCMA) is applied in an external bias field (\mathbf{B}^{ext}) of 0.3 T. **c** Schematic of qubit layers. Ferromagnet/Oxide interface to create perpendicular magnetic anisotropy (PMA) in the film (magnetized along $-z$) below the qubit volume. This field partially offsets the external field so the effective field along $+z$ seen by the qubit produces Larmor precession at 0.5 GHz (or 2 GHz). (Drawings are not to scale).

Table 1 List of parameters used in the simulation.

Parameters	Value
Saturation magnetization (\mathbf{M}_s)	$0.8 \times 10^6 \text{ Am}^{-1}$
Gilbert damping constant (α)	0.1
Exchange stiffness (A_{ex})	$10 \times 10^{-12} \text{ Jm}^{-1}$
Maximum PMA constant ($K_{\text{ul,max}}$)	$1.0 \times 10^6 \text{ Jm}^{-3}$
Exchange bias field ($B_{\text{bias},x}^{\text{ext}}$)	100 mT
Nanomagnet thickness (t)	1 nm
VCMA frequency (ν)	500 MHz and 2 GHz
VCMA coefficient (η)	$500 \text{ fJV}^{-1}\text{m}^{-1}$

drives the spins at resonant condition for a particular value of the effective magnetic bias field in the z -direction (due to the effective global bias magnetic field).

A ferromagnet/oxide interface below the qubit volume plays two roles. It creates a PMA in the film, which is magnetized to point along $-z$ axis that cancels part of the external magnetic bias field along $+z$ to produce an effective field which corresponds to the Larmor precession of the spins in the qubit volume at 0.5 GHz (or 2 GHz). The qubit volume can also be initialized by applying a spin-transfer-torque (STT) current where the MgO acts as a tunnel barrier layer.

The parameters used in the simulations are listed in Table 1. The effective bias magnetic field applied in the nanomagnet accounts for an external bias field of 0.3 T along the z -direction and the field along the z -direction due to PMA.

Induced field profiles. We simulated and obtained the magnetic field in the qubit volume for two cases: for a single nanomagnet and for two nanomagnets. The histogram plots in Fig. 2 show magnetic field gradients in both the x and z directions with a single nanomagnet and with two nanomagnets. The row and column numbers in the x and y axis correspond to the position of the spin in the qubit volume. In Fig. 2a and b, the maximum induced magnetic field along the x -axis $B_{\text{max},x}$ and the z -axis $B_{\text{max},z}$ are given for each of the 25 cells considered in the qubit volume for the case of a single nanomagnet. The maximum

amplitude achieved is 0.007 T and the field gradient is 0.003 T or 42.86% in the x -direction. This field gradient creates inhomogeneity and leads to low fidelity of quantum gate operations. The simulation result shows a reduced magnetic field gradient and improved amplitude in both x and z directions with two nanomagnets. The maximum amplitude $B_{\text{max},x}$ achieved is 0.011 T which is comparatively higher, and the field gradient is 0.001 T or 9.09%, which is comparatively lower than for the case with a single nanomagnet.

The VCMA-induced sinusoidal variation of PMA, magnetization dynamics due to this PMA variation, and time varying magnetic field in the qubit volume due to this magnetization dynamics are shown in Fig. 3 along with corresponding frequency domain plots. A purely sinusoidal PMA variation of 500 MHz is shown in time domain and frequency domain in Fig. 3a,b. The magnetization in the nanomagnet (Fig. 3c) and the induced magnetic field (Fig. 3e) contains higher harmonics (1 GHz, 2 GHz etc.) due to the nonlinear response of the nanomagnet to VCMA as shown in Fig. 3d,f. The magnetization of the nanomagnet pointing in the $+z$ axis induces a magnetic field in negative z direction due to the dipole effect.

The induced magnetic field (B_x, B_y, B_z) in the qubit volume in response to a 2 GHz sinusoidal VCMA applied in the nanomagnets and its frequency domain plot are shown in Fig. 4. The x -component (B_x) contains 2 GHz as well as higher order harmonics such as 4 GHz, 6 GHz etc.

For a single frequency control pulse, perfect gate implementation is possible in theory. It can be shown that as other harmonics add to the control field, reaching the same clean rotations become more challenging and we expect a drop in the gate fidelity as the number of Fourier components increases. Fourier decomposition is performed for the induced magnetic field at 500 MHz and 2 GHz (see Methods section IV.B). Since the 2 GHz field has a smaller number of components we expect gate operations with larger fidelities in comparison with the 500 MHz drive.

Spin dynamics. We show how to use the induced field of a nanomagnet for implementation of single-qubit gates on electron-spin qubits. By describing the evolution of spins, we

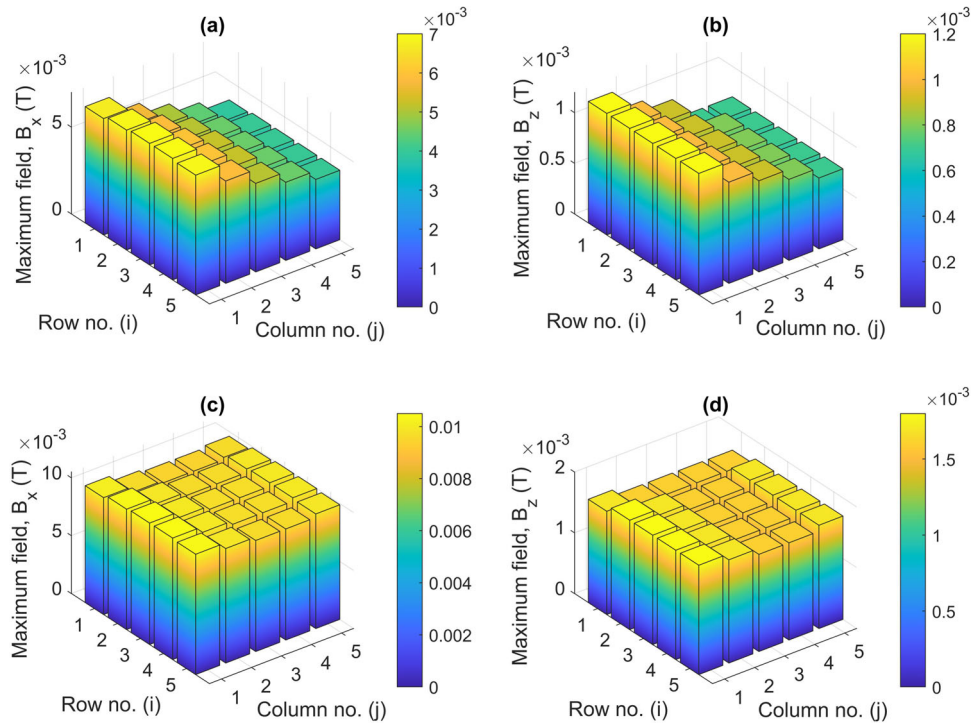


Fig. 2 Histogram of induced magnetic field along x - and z -axes in the qubit volume. **a** Maximum magnetic field of each spin along x (B_x), and **b** along z (B_z), induced by a single nanomagnet. **c** Maximum magnetic field of each spin along x (B_x), and **d** along z (B_z), induced in the dual nanomagnet setup. The color map indicates low (blue) and high (yellow) induced field.

show that despite the complex nature of the induced field profile, robust implementation of quantum gates is achievable.

The Hamiltonian, $\mathcal{H}(t) = -\gamma_e \mathbf{B}(t) \cdot \mathbf{S}$, for spin interaction with a magnetic field $\mathbf{B}(t) = \mathbf{B}_0 + \mathbf{B}_1(t)$ is

$$\begin{aligned} \mathcal{H}(t) &= -\omega_{1x}(t)\hat{S}_x - \omega_{1y}(t)\hat{S}_y - (\omega_0 + \omega_{1z}(t))\hat{S}_z \\ &= -(\omega_{1x}^{\text{st}} + \omega_{1x}^{\text{var}}(t))\hat{S}_x - (\omega_{1y}^{\text{st}} + \omega_{1y}^{\text{var}}(t))\hat{S}_y \\ &\quad - (\omega_0 + \omega_{1z}^{\text{st}} + \omega_{1z}^{\text{var}}(t))\hat{S}_z \\ &= \mathcal{H}_0 + \mathcal{H}_1(t) \end{aligned}$$

where $\omega_0 = \gamma_e B_0 \hat{z}$ is the angular velocity of electron spins (the Larmor frequency) when subjected to the external static field \mathbf{B}_0 , γ_e is the gyromagnetic ratio of the electron and $\omega_{1\alpha}(t) = \gamma_e \mathbf{B}_1(t) \cdot \hat{\alpha}$ for $\hat{\alpha} \in \{\hat{x}, \hat{y}, \hat{z}\}$, is proportional to the strength of the control field in each direction. The time-independent portion of the Hamiltonian $\mathcal{H}_0 = -\omega_{1x}^{\text{st}}\hat{S}_x - \omega_{1y}^{\text{st}}\hat{S}_y - (\omega_0 + \omega_{1z}^{\text{st}})\hat{S}_z$ includes the external field \mathbf{B}_0 and the time-independent part of the nanomagnet induced field \mathbf{B}_1^{st} . This is a result of the bias field applied to fix the rotation direction of the magnetization vector in the nanomagnet. $\mathcal{H}_1(t) = -\omega_{1x}^{\text{var}}(t)\hat{S}_x - \omega_{1y}^{\text{var}}(t)\hat{S}_y - \omega_{1z}^{\text{var}}(t)\hat{S}_z$ represents the time-dependent part of the induced magnetic field, which is used to control qubits, in place of radio frequency (RF) or microwave pulses.

Spin dynamics in the lab frame, is described with the Liouville von-Neumann equation, Eq. (4), with a unitary propagator defined as

$$U_1 = \tau \exp \left\{ -i \int_0^t [\mathcal{H}_0 + \mathcal{H}_1(t')] dt' \right\} \quad (1)$$

where τ is the Dyson time ordering operator.

The induced magnetic field of nanomagnet has a pronounced static field along x and z directions. These time-independent field components are part of the \mathcal{H}_0 Hamiltonian and as a result, the spins precess around an effective field defined by these fields,

which is in the $x - z$ plane, slightly deviating from the z -axis. The angular velocity for this precession is

$$\omega_r = \sqrt{(\omega_{1x}^{\text{st}})^2 + (\omega_{1z}^{\text{st}} + \omega_0)^2}.$$

Time-independent components of the induced field, ω_{1x}^{st} and ω_{1z}^{st} are evaluated using the time average of field components. Considering that ω_r should be in resonance with the drive frequency of the nanomagnet, the amplitude of the static external field is chosen such that ω_0 satisfies this equation.

The unitary propagator is evaluated for the continuous application of drive voltage using Eq. (1). Spin evolution shows the step-wise rotation of spins modulated with the rotation along the effective field with angular velocity ω_r . Depiction of spin dynamics is done by initializing one electron spin along the x , y , and z axes and projecting it on the x , z , and y axes after its rotation. Figure 5 shows the average observed signal for both drive frequencies at 500 MHz and 2 GHz. Since the largest time-dependent field component is along x , as we apply these pulse segments in resonance with the Larmor frequency of electron spin, we observe x rotations. As expected, the density matrix initialized along the x -axis only precess around the effective field with no change in time. Density matrices initialized in the $y - z$ plane, on the other hand, are affected by the x rotations.

These results are similar to the spin rotations in the traditional magnetic resonance experiments where spin control is implemented using RF pulses in resonance with the Larmor frequency of the spins in the external magnetic field. In the 2 GHz drive example, since the spin rotation happens in smaller steps, there is a smoother transition and we have more control for single-qubit gate implementation. The $X/2$ gate which is a $\pi/2$ rotation along the x -axis can be achieved by stopping the drive when ρ_y rotates to $-z$, or equivalently when ρ_z rotates to y . This rotation happens at 3.872 ± 0.001 ns for 500 MHz case and

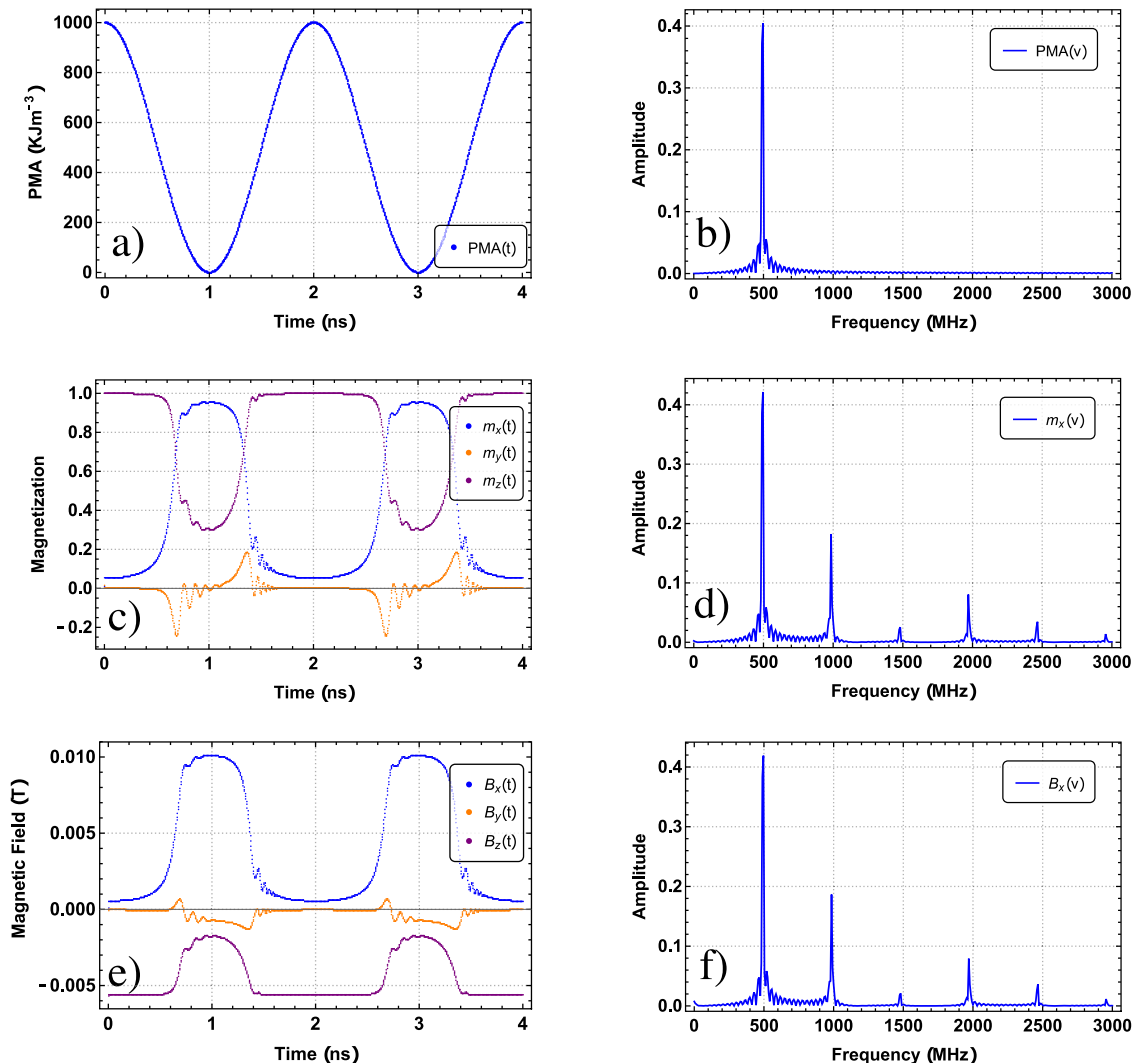


Fig. 3 Nanomagnet driven at 500 MHz. **a** Sinusoidal perpendicular magnetic anisotropy in the time domain and **b** in the frequency domain. Panels **c** and **d** show magnetization (m_x, m_y, m_z) of a nanomagnet in time and frequency domain, respectively. Panels **e** and **f** indicate induced magnetic field (B_x, B_y, B_z) in the qubit volume in time, and frequency domain, respectively.

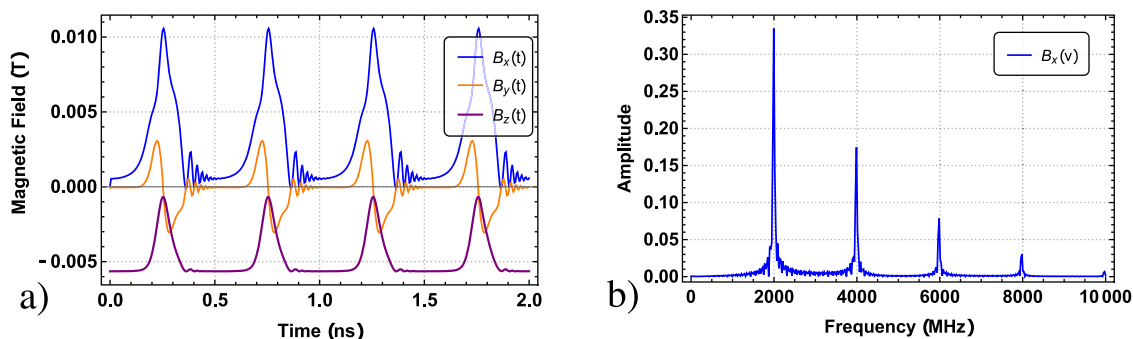


Fig. 4 Nanomagnet driven at 2 GHz. **a** Induced magnetic field (B_x, B_y, B_z) in the qubit volume in time domain, and **b** in frequency domain.

at 4.498 ± 0.001 ns in the case of 2 GHz drive. A sudden change of drive voltage, especially mid pulse, will cause oscillatory residual magnetic fields a.k.a. ringing effect. Ideally, we would like to implement gates that last an integer number of pulse segments to minimize the ringing effect. Rotations along the y -axis, or any other orientation in the $x-y$ plane, are implemented by shifting the phase of these X pulses, which is done by applying delays before the start of the pulse train. The

X gate is achieved at 7.882 ± 0.001 ns for 500 MHz and at 8.998 ± 0.001 ns for 2 GHz. Figure 6 shows the field profile of two rotations necessary for the implementation of Clifford gates, for the 2 GHz drive case.

In quantum information processing, error correction codes are used to prevent the loss of quantum information due to imperfections of quantum control. The idea is that if the gates are implemented with enough fidelity or with acceptable error

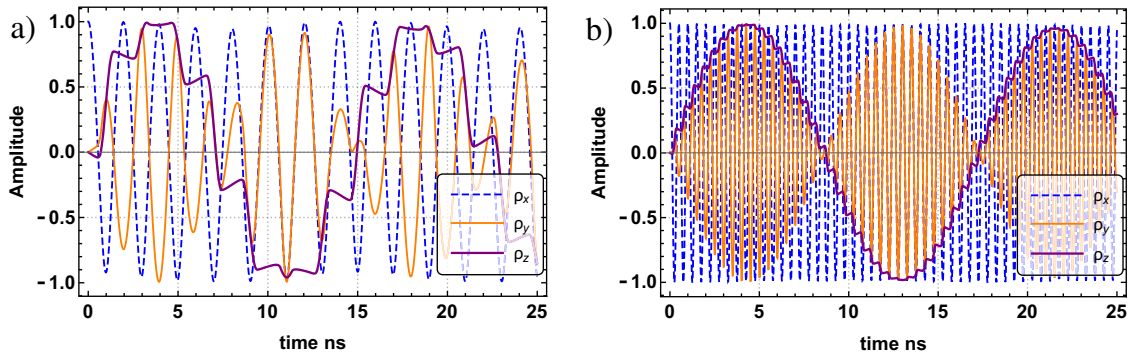


Fig. 5 Spin dynamics induced by nanomagnets. Evolution of 25 spins in the lab frame with the nanomagnet induced field at 500 MHz drive **a** and 2 GHz drive **b**. The dashed-blue line indicates the average projection of 25 spins on x axis when they were initialized along the x direction. The red (purple) line indicates the average projection on z (y) axis for spins initialized in the y (z) direction. The effective $(\pi/2)_x$ rotation happens at 3.871 ± 0.001 ns and 4.498 ± 0.001 ns in 500 MHz and 2 GHz drives, respectively. Spins rotate a π radian along the x-axis at 7.882 ± 0.001 ns and 8.998 ± 0.001 ns in 500 MHz and 2 GHz frequencies, respectively.

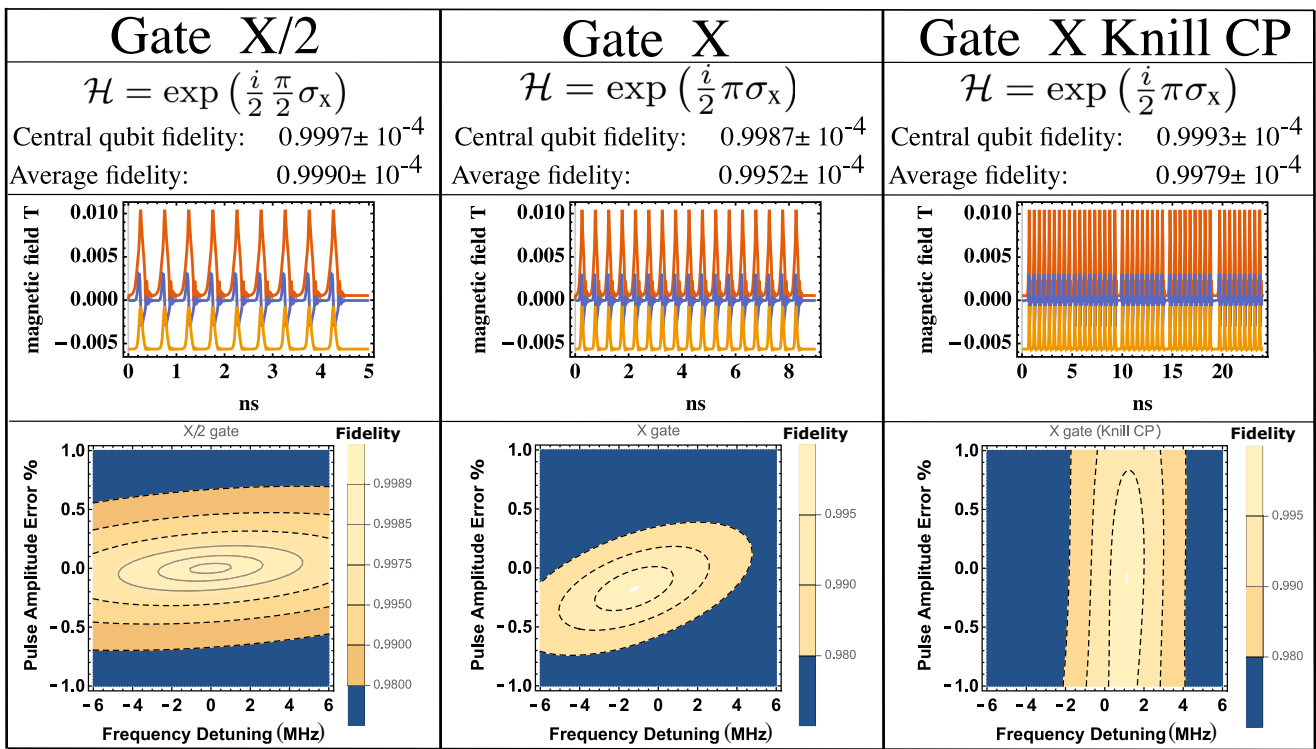


Fig. 6 Implementation of quantum gates using nanomagnets driven at 2 GHz. Each column represents the one-qubit gate indicated in the first row. The second row shows the gate fidelity for the central qubit along with the average fidelity for gate implementation for all 25 qubits at the qubit volume. The uncertainty in fidelity is estimated based on variations (spatial inhomogeneity) of the effective field. The third row is a depiction of the induced magnetic field profile for the central qubit, where B_x , B_y , B_z components are presented with red, blue and orange lines, respectively. The fourth row indicates contour plots of average gate fidelity, evaluated for frequency detuning and pulse amplitude errors. The color bar shows the average gate fidelity in each contour and the solid lines circumscribe the area where the error per gate is smaller than 3×10^{-3} .

probability per gate (or simply error per gate, EPG), they can be effectively used for quantum information processing. This threshold for EPG is determined by further assumptions of the error model and device parameters and is often between 10^{-6} and 3×10^{-3} (see refs. ^{9,54–56}). The typical value used as a threshold for the experimental implementation of quantum computers is the EPG of less than 10^{-4} ⁵⁷. In the case of two-level systems, average gate fidelity can be computed by comparing the ideal and noisy implementation of unitary maps ⁵⁸. For a general, linear, and trace-preserving map \mathcal{M} , and its ideal counterpart unitary U , the gate fidelity averaged over initial states is defined in terms of the

Hilbert-Schmidt inner product

$$\bar{F} = \frac{1}{2} + \frac{1}{3} \sum_{j=x,y,z} \text{Tr} \left[U \frac{\sigma_j}{2} U^\dagger \mathcal{M} \left(\frac{\sigma_j}{2} \right) \right]. \quad (2)$$

As indicated in Fig. 6, the fidelity of the X/2 gate implemented by the nanomagnet, is close to the required EPG threshold at $99.97 \pm 0.01\%$. This fidelity value applies to a single spin located at the center of the qubit volume. When the qubit has a finite volume, the fidelity will degrade due to field inhomogeneities over the volume. To assess the impact of inhomogeneities, we view the fidelity as a function of position

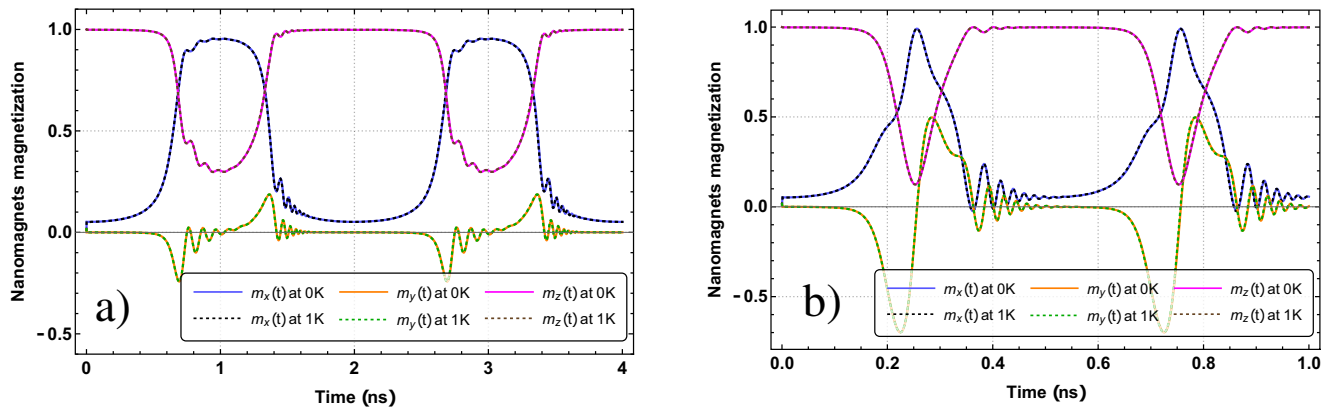


Fig. 7 Effect of thermal noise on the nanomagnets. Magnetization of the nanomagnet at 0 K and 1 K, **a** driven at 500 MHz and **b** 2 GHz.

(i.e. $\bar{F} \equiv \bar{F}(\mathbf{r})$) and average over the lattice sites:

$$\langle \bar{F} \rangle_{\Omega} = \frac{1}{N} \sum_{\mathbf{r}_i \in \Omega} \bar{F}(\mathbf{r}_i)$$

where Ω is the set of lattice points, $\bar{F}(\mathbf{r}_i)$ is the fidelity of the gate at lattice site $\mathbf{r}_i \in \Omega$ and $N = |\Omega|$ is the number of lattice sites. For the $X/2$ gate the volume averaged fidelity drops to $99.90 \pm 0.01\%$. The fidelity for the longer X gate ($99.87 \pm 0.01\%$ at the central spin), on the other hand, falls short of the required threshold. Longer pulses may be improved by using composite pulses that compensate locally for errors in the rotation angles. This is a well-established method in nuclear magnetic resonance for the design of robust pulses^{59,60}. The so-called Knill pulse is a composite π pulse designed specifically to be robust against frequency offset and pulse amplitude fluctuation errors. It is a symmetric combination of the following five pulses

$$\pi_0^{\text{ideal}} \left(\frac{\pi}{3} \right)_z = (\pi)_{\frac{\pi}{6}} (\pi)_0 (\pi)_{\frac{\pi}{2}} (\pi)_0 (\pi)_{\frac{\pi}{6}}.$$

An X gate implemented with Knill composite pulse shows significant improvement and reaches a gate fidelity of $99.93 \pm 0.01\%$ at the central spin and $99.79 \pm 0.01\%$ when averaged over the designated qubit volume.

Volume averaging was done on a 2D planar lattice Ω consisting of $N = 25$ spins separated 1 nm apart. As expected, performance degrades compared to the case of 1 spin. This merely reflects the well-known fact that it is impossible to be perfectly on resonance with all the spins simultaneously. The B_1 inhomogeneity thus degrades the average gate fidelity. Although the resulting fidelities dip below the typical value for acceptable error rates, they remain reasonably close to it. A map of average gate fidelity for qubit volume, with frequency detuning of $\pm 0.3\%$ and pulse amplitude errors of $\pm 1\%$ is plotted in Fig. 6. The results show high fidelity regions that depict the robustness of our gates.

Conclusion

In conclusion, the use of nanoscale magnets allows the production of highly localized AC magnetic fields to implement single qubit gates. While not all nanomagnets end up identical during fabrication, variations in anisotropy can be shown to have a negligible effect on the results presented here when employing state-of-the-art lithographic processes. Despite the highly non-linear response of the magnetization of the nanoscale magnets to an electric field, we are able to achieve high single qubit gate fidelity through the appropriate use of robust composite pulses. The significance of using nanomagnets for quantum control is that we can achieve local control over spin qubits. The power

required to oscillate nanomagnets at 500 MHz and 2 GHz by voltage control is lower than that required to power a coil by current control.

We note that the two frequencies studied here were chosen to show flexibility of operation. The operating frequency of these nanomagnets could be increased by a few hundreds megahertz, but not much higher due to the dissipative properties of the magnets. Apart from qubit lifetime, there are no theoretical lower bounds on the minimum operating frequency. To control the spin ensemble, the limiting factor for driving the nanomagnet to higher frequencies is not the capacitance and resistance but the ferromagnetic resonance (FMR) frequency which can be increased up to 31 GHz⁶¹ with associated increase in non-linearity and higher harmonics. The FMR frequency of the nanomagnet ultimately limits the frequency of the AC control field. For example, a VCMA controlled nanomagnet with oxide barrier 1 nm thick and radius 50 nm would have a capacitance of 1.7×10^{-15} F and resistance of 2000 Ω ^{62,63}. This corresponds to an RC time constant of ~ 3.5 ps that enables operation at ~ 100 GHz while FMR limits operation to 31 GHz⁶¹. Also, no attempt was made here to optimize the results, as optimization efforts would depend on the details of qubits and architecture used. With some effort, the geometric arrangement could be improved, for example, to increase the homogeneity and/or minimize the stray field affecting neighboring qubits. The use of composite pulses allows for qubit control that is robust with respect to field inhomogeneity (Fig. 6). Combining the burgeoning spintronic field of energy efficient voltage control of magnetism with quantum computing with robust spin qubits, will stimulate further experiments in energy efficient, robust quantum computing devices at temperatures of a few K.

Methods

Micromagnetics. The simulations of the magnetization dynamics in the nanomagnets are performed by solving the LLG equation

$$\frac{d\mathbf{m}}{dt} = -\frac{\gamma \mathbf{m} \times \mathbf{H}_{\text{eff}}}{(1 + \alpha^2)} - \frac{\alpha \gamma \mathbf{m} \times (\mathbf{m} \times \mathbf{H}_{\text{eff}})}{(1 + \alpha^2)} \quad (3)$$

at 0 K using a micromagnetic framework (MuMax3⁶⁴). We note that single-qubit⁶⁵ and two-qubit⁶⁶ control is demonstrated at temperature above 1 K^{65–69} in silicon quantum dots and operation around 1 K does not introduce significant noise to alter the dynamics of the nanomagnet magnetization results presented herein (see Fig. 7). The root mean square (RMS) error of magnetization along the x -direction is only 0.0039 at 500 MHz and 0.0044 at 2 GHz. Here, α is the Gilbert damping coefficient, γ is the gyromagnetic ratio, $\mathbf{m} = \frac{\mathbf{M}}{M_s}$ is the normalized magnetization, where \mathbf{M} is the magnetization and M_s is the saturation magnetization. The effective magnetic field, \mathbf{H}_{eff} in this case consists of the fields due to the exchange interaction, uniaxial anisotropy of the nanomagnets, and the demagnetizing field.

$$\mathbf{H}_{\text{eff}} = \mathbf{H}_{\text{an}} + \mathbf{H}_{\text{ex}} + \mathbf{H}_{\text{d}}$$

where \mathbf{H}_{an} is the effective field due to the uniaxial perpendicular magnetic

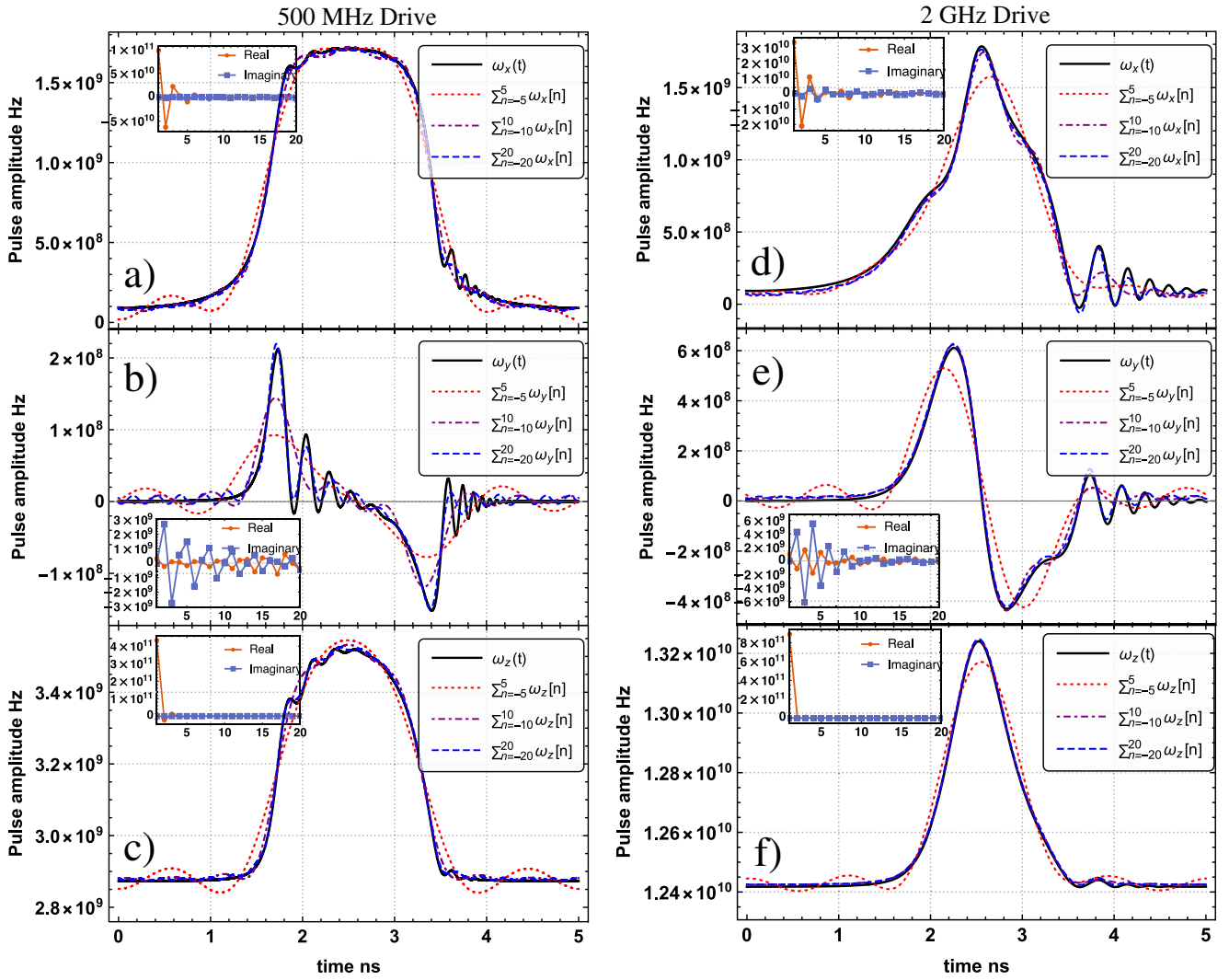


Fig. 8 Fourier components of induced magnetic field. x , y , and z component of the induced magnetic field with 500 MHz drive, are indicated in panels **a–c** respectively. Panels **d–f** are showing the results for 2 GHz drive. In each case Fourier components with $N = 5, 10, 20$ are used to reconstruct the original field profile. The first 20 Fourier coefficients of each field are plotted in the inset.

anisotropy (PMA) which can be modulated using voltage control of magnetic anisotropy (VCMA), \mathbf{H}_{ex} is the effective field due to Heisenberg exchange coupling and \mathbf{H}_d is the field due to the demagnetization energy (shape anisotropy).

The effective field due to the perpendicular magnetic anisotropy, \mathbf{H}_{an} is given as:

$$\mathbf{H}_{\text{an}} = \frac{2K_{u1}}{\mu_0 M_s} (\hat{z} \cdot \mathbf{m}) \hat{z}.$$

Here, the first order uniaxial anisotropy constant is K_{u1} , the magnetic permeability of free space is μ_0 , and \hat{z} is the unit vector corresponding to the anisotropy direction.

While PMA is created from the interaction between the ferromagnet's hybridized d_{xz} and oxygen's p_z orbital at a ferromagnet/oxide interface⁷⁰, by the application of voltage pulse, the interface electron density as well as perpendicular anisotropy can be changed⁷¹. This phenomenon is called VCMA^{72–74}.

The cell sizes are chosen to be 1 nm^3 , so that all dimensions are well within the limit of ferromagnetic exchange length calculated by $\sqrt{2A_{\text{ex}}/\mu_0 M_s^2} \approx 4.99 \text{ nm}$.

Quantum control with periodic, polychromatic, inhomogeneous field. Spin dynamics in magnetic resonance experiments is governed by the time-dependent part of the Hamiltonian resulting from the application of RF pulses. Consider the Zeeman interaction between spin \mathbf{S} and external static field ($\mathbf{B}_0 = B_0 \hat{z} = (\omega_0/\gamma) \hat{z}$, where γ : gyromagnetic ratio, $g\mu_B/h$ for electrons or $g_n\mu_N/h$ for nuclei) and also time-dependent RF fields

$$\mathbf{B}_1(t) = (\omega_x(t)/\gamma) \hat{x} + (\omega_y(t)/\gamma) \hat{y} + (\omega_z(t)/\gamma) \hat{z}$$

is:

$$\begin{aligned} \mathcal{H}(t) &= -\gamma(\mathbf{B}_0 + \mathbf{B}_1(t)) \cdot \mathbf{S} \\ &= -\omega_x(t) \hat{S}_x - \omega_y(t) \hat{S}_y - (\omega_0 + \omega_z(t)) \hat{S}_z \\ &= \mathcal{H}_0 + \mathcal{H}_1(t) \end{aligned}$$

where

$$\mathcal{H}_0 = -\omega_0 \hat{S}_z, \quad \mathcal{H}_1(t) = -(\omega_x(t) \hat{S}_x + \omega_y(t) \hat{S}_y + \omega_z(t) \hat{S}_z).$$

Denoting operators transformed to the rotating frame by a tilde, we write:

$$\tilde{\mathcal{H}}(t) = e^{i\omega_0 \hat{S}_z t} \mathcal{H}(t) e^{-i\omega_0 \hat{S}_z t}$$

$$\tilde{\rho}(t) = e^{i\omega_0 \hat{S}_z t} \rho(t) e^{-i\omega_0 \hat{S}_z t}$$

By differentiating the latter expression with respect to time, we find the evolution of density matrix in the interaction representation, a.k.a. Liouville von-Neumann equation:

$$\frac{\partial \tilde{\rho}}{\partial t} = -i[\tilde{\mathcal{H}}(t), \tilde{\rho}(t)] \quad (4)$$

where

$$\begin{aligned} \tilde{\mathcal{H}}(t) &= \tilde{\mathcal{H}}_0 + \tilde{\mathcal{H}}_1(t) - \omega_0 \hat{S}_z \\ &= e^{i\omega_0 \hat{S}_z t} [-\omega_x(t) \hat{S}_x - \omega_y(t) \hat{S}_y] e^{-i\omega_0 \hat{S}_z t} + \end{aligned} \quad (5)$$

$$(-\omega_0 - \omega_z(t) + \omega_r) \hat{S}_z \quad (6)$$

The solution to Eq. (4) is given in terms of time-ordered exponentials:

$$\tilde{\rho}(t) = \mathcal{T} e^{-i \int_0^t \tilde{H}(t') dt'} \tilde{\rho}(0) \mathcal{T} e^{i \int_0^t \tilde{H}(t') dt'}$$

Consider a single frequency RF pulse

$$\omega_x(t) = w_1 \cos(\omega_r t + \phi(t)), \quad \omega_y(t) = w_1 \sin(\omega_r t + \phi(t))$$

and let $\omega_z(t) = 0$ for simplicity. At the resonance condition $\omega_0 = \omega_r$, the spin evolution in the interaction representation is described with

$$\tilde{H}(t) = e^{i\omega_0 \hat{S}_z t} w_1 \left[\cos(\omega_0 t + \phi(t)) \hat{S}_x - \sin(\omega_0 t + \phi(t)) \hat{S}_y \right] e^{-i\omega_0 \hat{S}_z t}. \quad (7)$$

This is a rotation with the Rabi frequency w_1 . We can extend the analogy for a periodic control field with period T , containing multiple frequencies, expressed as a sum over Fourier components

$$\omega_x(t) = \sum_{n_x=-N}^N c_x[n_x] e^{i2\pi n_x t/T}.$$

Here $f_0 = 1/T$ is the fundamental frequency and the coefficient in the Fourier space are defined as

$$c[n] = \frac{1}{T} \int_0^T \omega(t) e^{-i2\pi n t/T} dt.$$

Similar expressions also exist for y and z . Substitution into Eq. (6) gives:

$$\begin{aligned} \tilde{H}(t) &= e^{i\omega_0 \hat{S}_z t} \left[\omega_x(t) \hat{S}_x + \omega_y(t) \hat{S}_y \right] e^{-i\omega_0 \hat{S}_z t} \\ &+ (\omega_0 + \omega_z(t) - \omega_r) \hat{S}_z \\ &= \sum_{n=-N}^N e^{i\omega_0 \hat{S}_z t} \left(c_x[n] \hat{S}_x + c_y[n] \hat{S}_y \right) e^{i2\pi n t/T} e^{-i\omega_0 \hat{S}_z t} \\ &+ (\omega_0 + c_z[n] e^{i2\pi n t/T} - \omega_r) \hat{S}_z \end{aligned}$$

By setting the fundamental frequency $2\pi f_0 = \omega_r = \omega_0$ the control Hamiltonian becomes:

$$\tilde{H}(t) = \sum_{n=-N}^N e^{i\omega_0 \hat{S}_z t} \left(c_x[n] \hat{S}_x + c_y[n] \hat{S}_y \right) e^{i\omega_0 n t} e^{-i\omega_0 \hat{S}_z t} + c_z[n] e^{i\omega_0 n t} \hat{S}_z$$

Using the ladder operators, $\hat{S}_+ = \hat{S}_x + i\hat{S}_y$, and $\hat{S}_- = \hat{S}_x - i\hat{S}_y$, and $[\hat{S}_z, \hat{S}_\pm] = \pm \hat{S}_\pm$ we have

$$e^{i\omega_0 \hat{S}_z t} \hat{S}_\pm e^{-i\omega_0 \hat{S}_z t} = \hat{S}_\pm + [\hat{S}_z, \hat{S}_\pm] i\omega_0 t + \dots = \hat{S}_\pm e^{\pm i\omega_0 t},$$

and the Hamiltonian becomes:

$$\tilde{H}(t) = \sum_{n=-N}^N \hat{S}_+ e^{i\omega_0(n+1)t} c_+[n] + \hat{S}_- e^{i\omega_0(n-1)t} c_-[n] + c_z[n] e^{i\omega_0 n t} \hat{S}_z \quad (8)$$

where we used the shorthand notation:

$$c_+[n] := \frac{c_x[n]}{2} + \frac{c_y[n]}{2i}, \quad c_-[n] := \frac{c_x[n]}{2} - \frac{c_y[n]}{2i}.$$

The real parameters $c_\alpha[n]$ are the components of the control field oscillating at the Larmor frequency ω_0 . The component $c_z[0]$ is the time-average of the field (z component). If the z -component is sinusoidal, it has no d.c. component and $c_z[0] = 0$. If there is a d.c. offset (nonzero background field), this will cause a shift in the resonance frequency away from ω_0 by the amount $c_z[0]$.

The x , y and z components of one control pulse segment, induced by the nanomagnet at the 500 MHz and 2 GHz drive frequencies are shown in Fig. 8. For each direction α , Fourier components $\omega_\alpha[n] = c_\alpha e^{i2\pi n t/T}$, are added to reconstruct the original time-domain field profile. Notice that by adding higher number of Fourier components, a better approximation of the induced field is achieved. These components may be used in Eq. (8) to evaluate the unitary propagator for the periodic control field. From this we conclude that although the presence of harmonics (Fig. 8) in the control field introduces significant deviations from a sinusoid shape, the presence of an external field comparable to the peak B_1 field is sufficient to average away these components and yield a high gate fidelity. Normally, the rotating wave approximation is only applied in the limit of high fields.

Data availability

Data points used to construct the graphs can be obtained by contacting the lead authors (chowdhurymf@vcu.edu and mniknam@gmail.com).

Code availability

There is no custom code required to produce the results.

Received: 5 April 2022; Accepted: 13 October 2022;

Published online: 12 November 2022

References

- Monroe, C. et al. Programmable quantum simulations of spin systems with trapped ions. *Rev. Mod. Phys.* **93**, 025001 (2021).
- Ebadi, S. et al. Quantum phases of matter on a 256-atom programmable quantum simulator. *Nature* **595**, 227–232 (2021).
- Pla, J. J. et al. High-fidelity readout and control of a nuclear spin qubit in silicon. *Nature* **496**, 334–338 (2013).
- Cory, D. G., Fahmy, A. F. & Havel, T. F. Ensemble quantum computing by nmr spectroscopy. *Proc. Nat. Acad. Sci.* **94**, 1634–1639 (1997).
- Gershenfeld, N. A. & Chuang, I. L. Bulk spin-resonance quantum computation. *Science* **275**, 350–356 (1997).
- Lutchyn, R. M. et al. Majorana zero modes in superconductor–semiconductor heterostructures. *Nat. Rev. Mater.* **3**, 52–68 (2018).
- Arute, F. et al. Quantum supremacy using a programmable superconducting processor. *Nature* **574**, 505–510 (2019).
- Asaad, S. et al. Coherent electrical control of a single high-spin nucleus in silicon. *Nature* **579**, 205–209 (2020).
- Chatterjee, A. et al. Semiconductor qubits in practice. *Nat. Rev. Phys.* **3**, 157–177 (2021).
- Madzik, M. T. et al. Precision tomography of a three-qubit donor quantum processor in silicon. *Nature* **601**, 348–353 (2022).
- Pezzagna, S. & Meijer, J. Quantum computer based on color centers in diamond. *Appl. Phys. Rev.* **8**, 011308 (2021).
- Rugar, A. E. et al. Quantum photonic interface for tin-vacancy centers in diamond. *Phys. Rev. X* **11**, 031021 (2021).
- Nadj-Perge, S., Frolov, S., Bakkers, E. & Kouwenhoven, L. P. Spin-orbit qubit in a semiconductor nanowire. *Nature* **468**, 1084–1087 (2010).
- Pla, J. J. et al. A single-atom electron spin qubit in silicon. *Nature* **489**, 541–545 (2012).
- Yoneda, J. et al. A quantum-dot spin qubit with coherence limited by charge noise and fidelity higher than 99.9%. *Nat. Nanotechnol.* **13**, 102–106 (2018).
- Preskill, J. Fault-tolerant quantum computation. In *Introduction to quantum computation and information*, 213–269 (World Scientific, 1998).
- Gottesman, D. Theory of fault-tolerant quantum computation. *Phys. Rev. A* **57**, 127–137 (1998).
- Liu, L. et al. Spin-torque switching with the giant spin hall effect of tantalum. *Science* **336**, 555–558 (2012).
- Pai, C.-F. et al. Spin transfer torque devices utilizing the giant spin hall effect of tungsten. *Appl. Phys. Lett.* **101**, 122404 (2012).
- Niimi, Y. et al. Giant spin hall effect induced by skew scattering from bismuth impurities inside thin film cubi alloys. *Phys. Rev. Lett.* **109**, 156602 (2012).
- Maruyama, T. et al. Large voltage-induced magnetic anisotropy change in a few atomic layers of iron. *Nat. Nanotechnol.* **4**, 158–161 (2009).
- Shiota, Y. et al. Voltage-assisted magnetization switching in ultrathin fe80co20 alloy layers. *Appl. Phys. Express* **2**, 063001 (2009).
- Shiota, Y. et al. Induction of coherent magnetization switching in a few atomic layers of fcco using voltage pulses. *Nat. Mater.* **11**, 39–43 (2012).
- Grezes, C. et al. Ultra-low switching energy and scaling in electric-field-controlled nanoscale magnetic tunnel junctions with high resistance-area product. *Appl. Phys. Lett.* **108**, 012403 (2016).
- Rana, B. & Otani, Y. Towards magnonic devices based on voltage-controlled magnetic anisotropy. *Communications Physics* **2**, 90 (2019).
- Choudhury, S. et al. Voltage controlled on-demand magnonic nanochannels. *Sci Adv* **6** (2020).
- Atulasimha, J. & Bandyopadhyay, S. Bennett clocking of nanomagnetic logic using multiferroic single-domain nanomagnets. *Applied Physics Letters* **97**, 173105 (2010).
- Cui, J. et al. Generation of localized strain in a thin film piezoelectric to control individual magnetoelectric heterostructures. *Applied Physics Letters* **107**, 092903 (2015).
- D'Souza, N., Salehi Fashami, M., Bandyopadhyay, S. & Atulasimha, J. Experimental clocking of nanomagnets with strain for ultralow power boolean logic. *Nano. Lett.* **16**, 1069–1075 (2016).
- Mathurin, T. et al. Stress-mediated magnetoelectric control of ferromagnetic domain wall position in multiferroic heterostructures. *Appl. Phys. Lett.* **108**, 082401 (2016).
- Bandyopadhyay, S., Atulasimha, J. & Barman, A. Magnetic straintronics: Manipulating the magnetization of magnetostriuctive nanomagnets with strain for energy-efficient applications. *Appl. Phys. Rev.* **8**, 041323 (2021).
- Fabiha, R. et al. Spin wave electromagnetic nano-antenna enabled by tripartite phonon-magnon-photon coupling. *Adv. Sci.* **9**, 2104644 (2022).

33. Heron, J. et al. Electric-field-induced magnetization reversal in a ferromagnet-multiferroic heterostructure. *Phys. Review Lett.* **107**, 217202 (2011).
34. D'Souza, N. et al. Energy-efficient switching of nanomagnets for computing: straintronics and other methodologies. *Nanotechnology* **29**, 442001 (2018).
35. Wang, K. L., Lee, H. & Amiri, P. K. Magnetolectric random access memory-based circuit design by using voltage-controlled magnetic anisotropy in magnetic tunnel junctions. *IEEE Transactions Nanotechnol.* **14**, 992–997 (2015).
36. Nowak, J. J. et al. Dependence of voltage and size on write error rates in spin-transfer torque magnetic random-access memory. *IEEE Magnetics Lett.* **7**, 1–4 (2016).
37. Bhattacharya, D. et al. Creation and annihilation of non-volatile fixed magnetic skyrmions using voltage control of magnetic anisotropy. *Na Electron.* **3**, 539–545 (2020).
38. Bhattacharya, D., Al-Rashid, M. M. & Atulasimha, J. Voltage controlled core reversal of fixed magnetic skyrmions without a magnetic field. *Scientific reports* **6**, 1–6 (2016).
39. Rajib, M. M., Al Misba, W., Bhattacharya, D., Garcia-Sanchez, F. & Atulasimha, J. Dynamic skyrmion-mediated switching of perpendicular mtjs: Feasibility analysis of scaling to 20 nm with thermal noise. *IEEE Transactions on Electron Devices* **67**, 3883–3888 (2020).
40. Rajib, M. M., Misba, W. A., Bhattacharya, D. & Atulasimha, J. Robust skyrmion mediated reversal of ferromagnetic nanodots of 20 nm lateral dimension with high ms and observable dmi. *Sci. Reports.* **11**, 1–8 (2021).
41. Bhattacharya, D. & Atulasimha, J. Skyrmion-mediated voltage-controlled switching of ferromagnets for reliable and energy-efficient two-terminal memory. *ACS App. Materials Inter.* **10**, 17455–17462 (2018).
42. Labanowski, D. et al. Voltage-driven, local, and efficient excitation of nitrogen-vacancy centers in diamond. *Sci. Adv.* **4**, eaat6574 (2018).
43. Wang, X. et al. Electrical control of coherent spin rotation of a single-spin qubit. *npj Quantum Inform.* **6**, 1–6 (2020).
44. Mirkamali, M. S. & Cory, D. G. Mesoscopic spin systems as quantum entanglers. *Phys. Rev. A.* **101**, 032320 (2020).
45. Zhukov, A. A., Shapiro, D. S., Pogosov, W. V. & Lozovik, Y. E. Dynamics of a mesoscopic qubit ensemble coupled to a cavity: Role of collective dark states. *Phys. Rev. A.* **96**, 033804 (2017).
46. Barbara, B. Mesoscopic systems: classical irreversibility and quantum coherence. *Philosophical Transactions of the Royal Society A: Mathematical, Physical and Engineering Sci.* **370**, 4487–4516 (2012).
47. Gangloff, D. A. et al. Witnessing quantum correlations in a nuclear ensemble via an electron spin qubit. *Nat. Phys.* **17**, 1247–1253 (2021).
48. Giedke, G., Taylor, J. M., D'Alessandro, D., Lukin, M. D. & Imamoglu, A. Quantum measurement of a mesoscopic spin ensemble. *Phys. Rev. A.* **74**, 032316 (2006).
49. Beterov, I. I. et al. Coherent control of mesoscopic atomic ensembles for quantum information. *Laser Phys.* **24**, 074013 (2014).
50. Gangloff, D. A. et al. Witnessing quantum correlations in a nuclear spin ensemble via a proxy qubit. In *Quantum Information and Measurement VI 2021*, Tu3A.2 (Optica Publishing Group, 2021).
51. Jackson, D. M. et al. Quantum sensing of a coherent single spin excitation in a nuclear ensemble. *Nature Physics* **17**, 585–590 (2021).
52. Rabl, P. et al. Hybrid quantum processors: Molecular ensembles as quantum memory for solid state circuits. *Phys. Rev. Lett.* **97**, 033003 (2006).
53. Bhattacharya, D. & Atulasimha, J. Skyrmion-mediated voltage-controlled switching of ferromagnets for reliable and energy-efficient two-terminal memory. *ACS Applied Materials & Inter.* **10**, 17455–17462 (2018).
54. Knill, E. Quantum computing with realistically noisy devices. *Nature* **434**, 39–44 (2005).
55. Veldhorst, M. et al. An addressable quantum dot qubit with fault-tolerant control-fidelity. *Nat. Nanotechnol.* **9**, 981–985 (2014).
56. Wolfowicz, G. & Morton, J. Pulse techniques for quantum information processing. *eMagRes* **5**, 1515–1528 (2016).
57. Gottesman, D. *Stabilizer codes and quantum error correction* (California Institute of Technology, 1997).
58. Bowdrey, M. D., Oi, D. K., Short, A. J., Banaszek, K. & Jones, J. A. Fidelity of single qubit maps. *Physics Letters A* **294**, 258–260 (2002).
59. Levitt, M. H. Composite pulses. *Progress in Nuclear Magnetic Resonance Spectroscopy* **18**, 61–122 (1986).
60. Ryan, C. A., Hodges, J. S. & Cory, D. G. Robust decoupling techniques to extend quantum coherence in diamond. *Phys. Rev. Lett.* **105**, 200402 (2010).
61. Skowronski, W. et al. High frequency voltage-induced ferromagnetic resonance in magnetic tunnel junctions. *Applied Physics Letters* **115**, 072401 (2019).
62. Wang, M. et al. Current-induced magnetization switching in atom-thick tungsten engineered perpendicular magnetic tunnel junctions with large tunnel magnetoresistance. *Nat. Commun.* **9**, 1–7 (2018).
63. Zhang, X. et al. Skyrmions in magnetic tunnel junctions. *ACS Applied Materials & Interfaces.* **10**, 16887–16892 (2018).
64. Vansteenkiste, A. et al. The design and verification of mumax3. *AIP Adv.* **4**, 107133 (2014).
65. Yang, C. H. et al. Operation of a silicon quantum processor unit cell above one kelvin. *Nature* **580**, 350–354 (2020).
66. Petit, L. et al. Universal quantum logic in hot silicon qubits. *Nature* **580**, 355–359 (2020).
67. Vandersypen, L. et al. Interfacing spin qubits in quantum dots and donors—hot, dense, and coherent. *npj Quantum Inform.* **3**, 1–10 (2017).
68. Arroyo-Camejo, S., Lazariév, A., Hell, S. W. & Balasubramanian, G. Room temperature high-fidelity holonomic single-qubit gate on a solid-state spin. *Nat. Commun.* **5**, 1–5 (2014).
69. Ono, K., Mori, T. & Moriyama, S. High-temperature operation of a silicon qubit. *Sci. Reports.* **9**, 1–8 (2019).
70. Yang, H. X. et al. First-principles investigation of the very large perpendicular magnetic anisotropy at fe/mgo and colmgo interfaces. *Phys. Rev. B.* **84**, 054401 (2011).
71. Niranjana, M. K., Duan, C.-G., Jaswal, S. S. & Tsymbal, E. Y. Electric field effect on magnetization at the fe/mgo(001) interface. *App. Phys.Lett.* **96**, 222504 (2010).
72. AMIRI, P. K. & WANG, K. L. Voltage-controlled magnetic anisotropy in spintronic devices. *SPIN* **02**, 1240002 (2012).
73. Wang, W.-G., Li, M., Hageman, S. & Chien, C. Electric-field-assisted switching in magnetic tunnel junctions. *Nat. Mater.* **11**, 64–68 (2012).
74. Li, X., Lee, A., Razavi, S. A., Wu, H. & Wang, K. L. Voltage-controlled magnetoelectric memory and logic devices. *MRS Bulletin.* **43**, 970–977 (2018).

Acknowledgements

J.A., M.F.C., and M.M.R. were supported in part by National Science Foundation (NSF) grants 1815033 and 1909030. The research at UCLA was partially supported by NSF awards 2137984 and 1936375. J.A., M.F.C., L.S.B., M.N. also acknowledge support from NSF expandQISE grant 2231356.

Author contributions

J.A., K.L.W., R.N.S., and L.S.B. conceived the idea. All authors discussed the results and commented on the paper. J.A. defined the nanomagnet magnetization control and field inhomogeneity problem and M.F.C. performed the micromagnetic simulations with help from M.M.R. and W.A.M. L.S.B. defined the spin evolution problem and M.N. performed the spin dynamics simulations and quantum gate calculations. J.A., M.F.C., L.S.B. and M.N. wrote the paper.

Competing interests

The authors declare no competing interests.

Additional information

Correspondence and requests for materials should be addressed to Jayasimha Atulasimha or Louis-S. Bouchard.

Peer review information *Communications Physics* thanks the anonymous reviewers for their contribution to the peer review of this work.

Reprints and permission information is available at <http://www.nature.com/reprints>

Publisher's note Springer Nature remains neutral with regard to jurisdictional claims in published maps and institutional affiliations.



Open Access This article is licensed under a Creative Commons Attribution 4.0 International License, which permits use, sharing, adaptation, distribution and reproduction in any medium or format, as long as you give appropriate credit to the original author(s) and the source, provide a link to the Creative Commons license, and indicate if changes were made. The images or other third party material in this article are included in the article's Creative Commons license, unless indicated otherwise in a credit line to the material. If material is not included in the article's Creative Commons license and your intended use is not permitted by statutory regulation or exceeds the permitted use, you will need to obtain permission directly from the copyright holder. To view a copy of this license, visit <http://creativecommons.org/licenses/by/4.0/>.

© The Author(s) 2022